

# Learning Domain-Invariant Representations for Cross-Domain Image Registration via Scene-Appearance Disentanglement

Jiahao Qin and Yiwen Wang<sup>\*</sup>

## Abstract

Image registration under domain shift remains a fundamental challenge in computer vision and medical imaging: when source and target images exhibit systematic intensity differences, the brightness constancy assumption underlying conventional registration methods is violated, rendering correspondence estimation ill-posed. We propose SAR-Net, a unified framework that addresses this challenge through principled scene-appearance disentanglement. Our key insight is that observed images can be decomposed into domain-invariant scene representations and domain-specific appearance codes, enabling registration via re-rendering rather than direct intensity matching. We establish theoretical conditions under which this decomposition enables consistent cross-domain alignment (Proposition 1) and prove that our scene consistency loss provides a sufficient condition for geometric correspondence in the shared latent space (Proposition 2). Empirically, we validate SAR-Net on bidirectional scanning microscopy, where coupled domain shift and geometric distortion create a challenging real-world testbed. Our method achieves 0.885 SSIM and 0.979 NCC, representing 3.1 $\times$  improvement over the strongest baseline, while maintaining real-time performance (77 fps). Ablation studies confirm that both scene consistency and domain alignment losses are necessary: removing either degrades performance by 90% SSIM or causes 223 $\times$  increase in latent alignment error, respectively. Code and data are available at <https://github.com/D-ST-Sword/SAR-NET>.

## 1 Introduction

Image registration—establishing spatial correspondence between images—is fundamental to computer vision, medical imaging, and scientific measurement [9, 21]. Classical registration methods, from optical flow [14] to diffeomorphic algorithms [11, 24], share a common assumption: *brightness constancy*, which posits that corresponding points have similar intensities across images. This assumption, however, is violated in numerous practical scenarios where images undergo *domain shift*—systematic intensity transformations arising from varying acquisition conditions, sensor characteristics, or imaging physics.

The coupling of domain shift with geometric misalignment creates a chicken-and-egg problem: accurate registration requires intensity correspondence, yet establishing correspondence requires prior alignment. This challenge manifests across diverse applications, including multi-modal medical imaging [23], satellite imagery under varying illumination [9], and high-speed microscopy with direction-dependent acquisition artifacts.

We study this problem through the lens of *disentangled representation learning* [36, 37]. Our key hypothesis is that observed images admit a factorized representation:  $I = \mathcal{F}(S, A)$ , where  $S$  denotes domain-invariant *scene* content (geometry, structure) and  $A$  captures domain-specific *appearance*

---

<sup>\*</sup>Jiahao Qin and Yiwen Wang contributed equally to this work.

<sup>†</sup>E-mail: jiahao.qin19@gmail.com; ywwang25@m.fudan.edu.cn

(intensity characteristics). Under this formulation, registration reduces to alignment in the shared scene space, circumventing brightness constancy violations in image space.

**Motivating application.** We ground our investigation in high-speed bidirectional scanning microscopy, specifically optical-resolution photoacoustic microscopy (OR-PAM) [1, 5]. Bidirectional scanning doubles imaging speed but introduces coupled artifacts at intra-frame and inter-frame levels, providing a challenging real-world testbed for our framework.

**Problem formalization.** Let  $I_{\text{odd}}, I_{\text{even}} \in \mathbb{R}^{H \times W}$  denote paired acquisitions of the same underlying scene  $S$  under different imaging conditions. The observed images follow distinct imaging operators:

$$I_{\text{odd}} = \mathcal{F}_{\text{odd}}(S), \quad I_{\text{even}} = \mathcal{F}_{\text{even}}(S). \quad (1)$$

Critically,  $\mathcal{F}_{\text{odd}} \neq \mathcal{F}_{\text{even}}$  due to two coupled factors: (1) *geometric misalignment*  $\phi : \mathbb{R}^2 \rightarrow \mathbb{R}^2$ , and (2) *domain shift*  $\mathcal{T} : \mathbb{R} \rightarrow \mathbb{R}$ , a nonlinear intensity transformation. The composite degradation  $I_{\text{even}} = \mathcal{T}(S \circ \phi)$  violates brightness constancy  $I_{\text{odd}}(x) \approx I_{\text{even}}(\phi(x))$ , rendering conventional registration ill-posed.

**Temporal extension.** For sequences  $\{I^{(t)}\}_{t=1}^T$ , both scene  $S^{(t)}$  and imaging operator  $\mathcal{F}^{(t)}$  evolve over time. The non-stationary distribution  $p(I^{(t)}|S^{(t)}, \mathcal{F}^{(t)})$  precludes direct frame-to-frame correspondence, as neither brightness constancy nor statistical stationarity holds across the sequence.

**Limitations of existing approaches.** Current methods fall into two categories, both with fundamental limitations. *Registration-first* approaches [11, 25, 26] assume brightness constancy, failing when domain shift confounds correspondence. *Translation-first* approaches using cycle-consistent GANs [29, 30] preserve global content but lack geometric guarantees, allowing local spatial distortions. Neither paradigm provides principled joint treatment of domain shift and spatial alignment.

**Our approach.** We propose SAR-Net (Scene-Appearance Registration Network), a unified framework grounded in the factorization  $I = \mathcal{F}(S, A)$ . Rather than directly matching intensities or warping pixels, we learn to: (1) invert the imaging process to recover  $(S, A)$  from observations, and (2) re-render the scene under target appearance for registration. This reformulation enables registration in a domain-invariant latent space where brightness constancy naturally holds.

**Contributions.** Our main contributions are:

1. **Theoretical framework:** We formalize registration under domain shift as scene-appearance disentanglement and establish conditions for identifiable decomposition (Section 3.3).
2. **Algorithmic innovation:** We introduce a scene consistency loss that enforces geometric correspondence in latent space, providing a sufficient condition for cross-domain alignment without explicit spatial transformation estimation.
3. **Empirical validation:** On bidirectional scanning microscopy, SAR-Net achieves  $3.1 \times$  SSIM improvement over the strongest baseline with real-time inference (77 fps). Ablation studies validate the necessity of each component.

## 2 Related Work

### 2.1 High-Speed PAM and Bidirectional Scanning Artifacts

Photoacoustic microscopy has rapidly evolved as a powerful modality for *in vivo* imaging [1], with early OR-PAM systems achieving micrometer-scale spatial resolution but limited by slow scanning speeds [3, 4]. High-speed scanning mechanisms, including voice-coil actuators [6] and rotational scanners [2, 15–17], have substantially improved temporal resolution for functional imaging.

Bidirectional scanning [5, 6] further doubles imaging speed but introduces scan-direction-dependent artifacts. Existing solutions rely on post-hoc calibration [7, 8] or manual adjustment, which are time-consuming and insufficient under dynamic *in vivo* conditions. Deep learning methods have shown promise for PAM enhancement [18–20], but bidirectional artifact correction remains constrained by limited paired ground truth.

## 2.2 Image Registration under Domain Shift

Medical image registration establishes spatial correspondence for anatomical comparison and motion correction [9, 21, 22]. Classical approaches include intensity-based methods such as mutual information [23] and diffeomorphic algorithms like Demons [11] and SyN [24]. Deep learning methods such as VoxelMorph [25] enable fast registration, with extensions incorporating attention mechanisms [26] and contrast robustness [27]. However, these methods implicitly assume comparable intensity distributions between images—an assumption violated by scan-direction-dependent domain shift in bidirectional scanning, leading to unreliable correspondence estimation.

## 2.3 Disentangled Representation Learning

Disentangled representations, where independent factors of variation are separated into distinct latent dimensions, have emerged as a principled approach to domain-invariant learning [36]. Variational approaches including  $\beta$ -VAE [37] and FactorVAE [38] encourage independence through information-theoretic regularization. For image translation, MUNIT [30] and DRIT [31] decompose images into content and style codes, enabling cross-domain synthesis. However, these methods optimize for perceptual quality rather than geometric fidelity, and theoretical guarantees for disentanglement remain limited to specific generative models [39]. Our work connects disentanglement to registration by establishing that scene-appearance separation, under appropriate constraints, provides sufficient conditions for geometric correspondence.

## 2.4 Domain Adaptation and Joint Registration-Translation

Generative adversarial networks have enabled unpaired image translation: Pix2Pix [28] for paired data and CycleGAN [29] for unpaired settings. However, cycle consistency encourages global content preservation without guaranteeing local geometric consistency, allowing spatial distortions in fine structures. Recent joint approaches, such as SynthMorph [27] using synthetic contrast augmentation and diffusion-based methods [32], improve robustness but rely primarily on data augmentation rather than explicit domain shift modeling. Domain adaptation theory [42] provides bounds on target domain performance but assumes access to labeled source data, which is unavailable in our unsupervised setting. In contrast, our method directly addresses the intrinsic coupling between domain shift and spatial misalignment through principled scene-appearance separation under geometric constraints.

## 3 Method

A unified framework is presented for bidirectional OR-PAM image registration based on scene-appearance separation. The proposed method jointly corrects domain shift and geometric misalignment within a single end-to-end trainable network. The overall architecture is illustrated in Fig. 1.

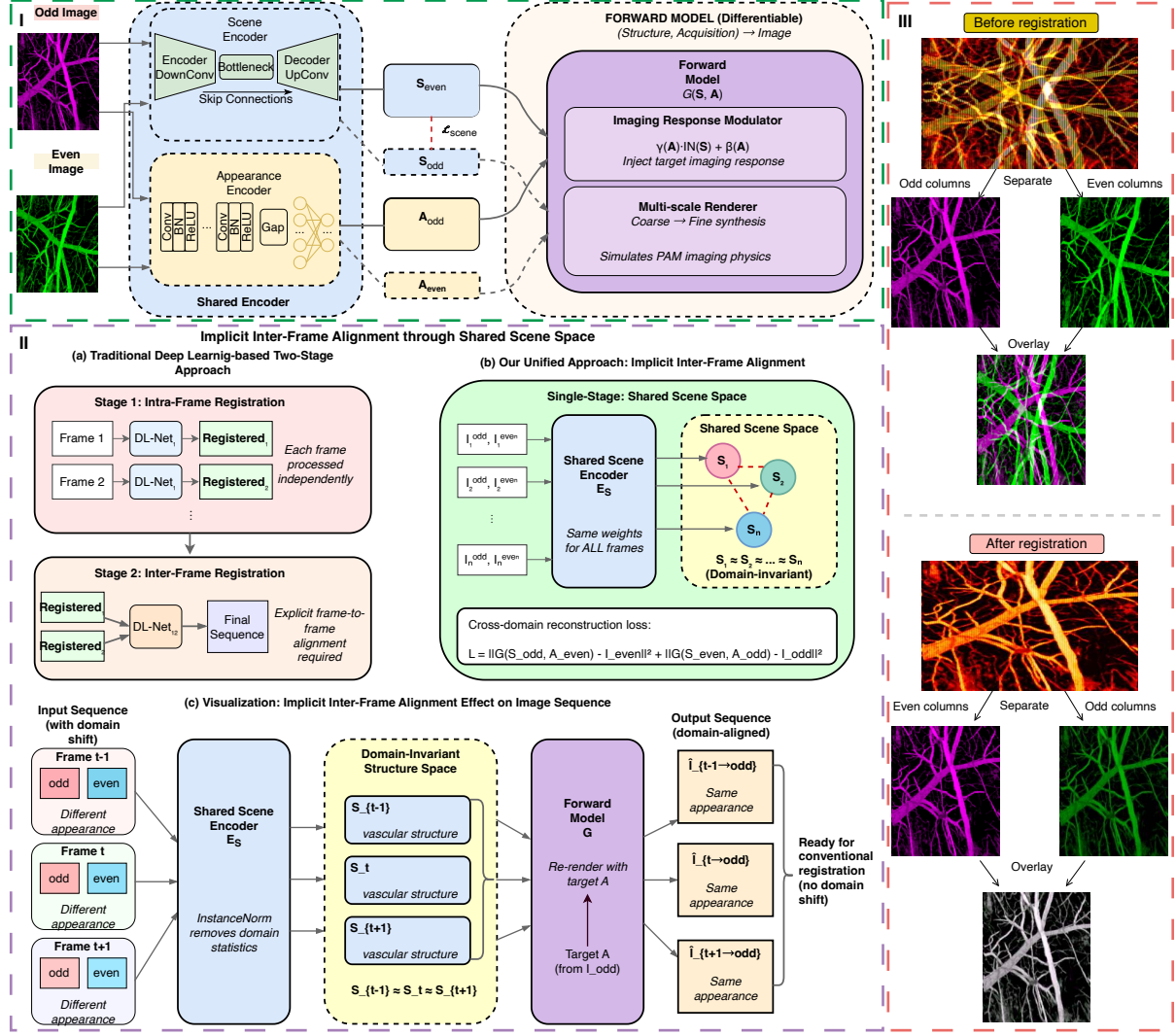


Figure 1: Overview of the proposed SAR-Net framework. **(I)** Network architecture: Scene Encoder  $E_S$  extracts domain-invariant anatomical structure using instance normalization; Appearance Encoder  $E_A$  captures domain-specific acquisition parameters via global average pooling; Forward Model  $G$  synthesizes images through feature modulation. The scene consistency loss  $\mathcal{L}_{\text{scene}}$  enforces geometric alignment between  $S_{\text{odd}}$  and  $S_{\text{even}}$ . **(II)** Comparison of registration pipelines: Conventional deep learning registration methods directly align images under brightness constancy assumptions, whereas our approach maps all frames to a shared scene space where  $S_1 \approx S_2 \approx \dots \approx S_n$ , enabling implicit inter-frame alignment without explicit frame-to-frame registration. **(III)** Registration results: Before/after comparison with odd-even overlay visualization (odd in magenta, even in green, alignment as white) demonstrating effective column alignment.

### 3.1 Problem Formulation: A Forward Modeling Perspective

A forward modeling perspective is adopted, motivated by the underlying physics of OR-PAM image formation. In bidirectional OR-PAM, the observed image  $I$  is determined by two independent factors: (1) the underlying anatomical structure  $S$ , and (2) the acquisition parameters  $A$ , which

encompass scan-direction-dependent imaging characteristics such as effective sampling conditions, intensity response, and system gain. The imaging process can be expressed as:

$$I = \mathcal{F}(S, A) + \epsilon, \quad (2)$$

where  $\mathcal{F}$  denotes the physical image formation process and  $\epsilon$  represents noise. Let  $\mathcal{D}_{\text{odd}}$  and  $\mathcal{D}_{\text{even}}$  denote the odd-line (forward) and even-line (backward) scanning domains, respectively. Both domains observe the same underlying structure  $S$  but under different acquisition parameters:

$$I_{\text{odd}} = \mathcal{F}(S, A_{\text{odd}}) + \epsilon_{\text{odd}}, \quad I_{\text{even}} = \mathcal{F}(S, A_{\text{even}}) + \epsilon_{\text{even}}. \quad (3)$$

This formulation highlights a key challenge in bidirectional OR-PAM: direct image registration is unreliable because the two images differ not only geometrically but also in acquisition conditions ( $A_{\text{odd}} \neq A_{\text{even}}$ ). Instead, we decompose the problem into two complementary tasks. The inverse problem aims to infer the domain-invariant structure  $S$  and domain-specific acquisition parameters  $A$  from the observed image  $I$ :

$$(S, A) = \mathcal{F}^{-1}(I). \quad (4)$$

While the forward problem corresponds to re-synthesizing an image by rendering the inferred structure under target acquisition conditions accordingly:

$$I_{\text{even} \rightarrow \text{odd}} = \mathcal{F}(S_{\text{even}}, A_{\text{odd}}) \approx I_{\text{odd}}. \quad (5)$$

From this perspective, cross-domain registration is equivalent to re-rendering: the shared structure is first extracted from the source domain and then rendered under the target domain's acquisition conditions. Conventional registration methods fail because they implicitly assume  $I_{\text{odd}} \approx T(I_{\text{even}})$  for some spatial transformation  $T$ , neglecting the fundamental domain shift induced by differing acquisition parameters.

### 3.2 Network Architecture: Implementing the Forward Model

The proposed framework implements the forward model (Eq. 2) through three key components: a Scene Encoder, an Appearance Encoder, and a Forward Model.

#### 3.2.1 Scene Encoder $E_S$

The Scene Encoder addresses the inverse problem of extracting domain-invariant anatomical structure from observed images. We adopt a U-Net architecture with instance normalization (IN) [33] as the key design choice. From a physical perspective, instance normalization removes channel-wise mean  $\mu$  and standard deviation  $\sigma$ , which encodes domain-specific intensity characteristics:

$$\text{IN}(x) = \frac{x - \mu(x)}{\sigma(x)}. \quad (6)$$

By normalizing these statistics, the encoder is encouraged to retain domain-invariant structural information shared across scanning directions. The network adopts an encoder–bottleneck–decoder architecture with skip connections:

$$S = E_S(I) \in \mathbb{R}^{C_S \times H \times W}, \quad (7)$$

where  $C_S = 64$  denotes the dimensionality of the structure feature. Skip connections preserve fine vascular details critical for accurate registration.

### 3.2.2 Appearance Encoder $E_A$

The Appearance Encoder extracts compact acquisition parameter codes that capture domain-specific characteristics. It consists of a lightweight convolutional network followed by global average pooling:

$$A = E_A(I) \in \mathbb{R}^{C_A}, \quad (8)$$

where  $C_A = 32$  denotes the acquisition code dimension. From a physical perspective, the acquisition parameters  $A$  encode scan-direction-dependent imaging responses. Global average pooling removes spatial information, ensuring that  $A$  captures scene-agnostic acquisition characteristics that affect the image globally rather than at specific spatial locations.

### 3.2.3 Forward Model $G$

The Forward Model implements the forward imaging equation  $I = \mathcal{F}(S, A)$  as a learnable neural network. We introduce an Imaging Response Modulator that applies domain-specific intensity characteristics to domain-invariant structure through feature modulation:

$$\text{Modulate}(S, A) = \gamma(A) \odot \text{IN}(S) + \beta(A), \quad (9)$$

where  $\gamma(A), \beta(A) \in \mathbb{R}^{C_S}$  are learned affine parameters (scale and shift) linearly derived from the acquisition code. From a physical perspective, the Imaging Response Modulator applies domain-specific intensity characteristics to domain-invariant structure representing the underlying biological anatomy. Mathematically, this operation can be interpreted as a transport of feature statistics in latent space, where the normalized feature distribution, characterized by  $(\mu, \sigma)$ , is mapped to the target domain-specific distribution. The parameters  $\gamma(A)$  model the contrast and gain response, while  $\beta(A)$  controls the intensity offset. The final synthesis can be shown as:

$$\hat{I} = G(S, A). \quad (10)$$

### 3.2.4 Cross-Domain Reconstruction as Re-Rendering

Cross-domain reconstruction follows a forward modeling perspective. Given images  $I_{\text{odd}}$  and  $I_{\text{even}}$  from two scanning domains, structure and acquisition parameters are first extracted:

$$\begin{aligned} S_{\text{odd}} &= E_S(I_{\text{odd}}), & A_{\text{odd}} &= E_A(I_{\text{odd}}), \\ S_{\text{even}} &= E_S(I_{\text{even}}), & A_{\text{even}} &= E_A(I_{\text{even}}). \end{aligned} \quad (11)$$

The forward problem can be solved through bidirectional cross-domain reconstruction:

$$I_{\text{even} \rightarrow \text{odd}} = G(S_{\text{even}}, A_{\text{odd}}), \quad I_{\text{odd} \rightarrow \text{even}} = G(S_{\text{odd}}, A_{\text{even}}). \quad (12)$$

From a physical perspective, cross-domain registration can be interpreted as a re-rendering process. The output  $I_{\text{even} \rightarrow \text{odd}}$  represents the anatomical structure extracted from the even-line image rendered under the odd-line domain's imaging characteristics. Unlike conventional registration, which directly warps pixel intensities, the proposed approach preserves geometric structure while transforming only the imaging response.

### 3.2.5 Implicit Inter-Frame Alignment via Shared Structure Space

A key property of the proposed framework is that it achieves implicit inter-frame alignment without explicit frame-to-frame registration. This property arises from the shared structure representation enforced by cross-domain reconstruction. We formalize this insight below.

### 3.3 Theoretical Analysis

We establish theoretical foundations for why scene-appearance disentanglement enables registration under domain shift.

**Proposition 1** (Cross-Domain Alignment via Re-Rendering). *Let  $G : \mathcal{S} \times \mathcal{A} \rightarrow \mathcal{I}$  be the forward model mapping scene-appearance pairs to images. Assume  $G$  is injective in its first argument, i.e., for fixed  $A$ ,  $G(S_1, A) = G(S_2, A) \Rightarrow S_1 = S_2$ . If cross-domain reconstruction achieves zero error:*

$$G(S_{\text{odd}}, A_{\text{even}}) = I_{\text{even}} = G(S_{\text{even}}, A_{\text{even}}), \quad (13)$$

then  $S_{\text{odd}} = S_{\text{even}}$  in the latent scene space.

*Proof.* By the injectivity assumption on  $G$  with respect to the scene argument, if  $G(S_{\text{odd}}, A_{\text{even}}) = G(S_{\text{even}}, A_{\text{even}})$  for the same appearance code  $A_{\text{even}}$ , then  $S_{\text{odd}} = S_{\text{even}}$ .  $\square$

Proposition 1 shows that successful cross-domain reconstruction implies scene consistency. However, optimizing reconstruction loss alone may lead to degenerate solutions. We next establish that the scene consistency loss provides stronger guarantees.

**Proposition 2** (Sufficiency of Scene Consistency). *Let  $E_S : \mathcal{I} \rightarrow \mathcal{S}$  be the scene encoder. If the scene consistency loss  $\mathcal{L}_{\text{scene}} = \|S_{\text{odd}} - S_{\text{even}}\|^2 \rightarrow 0$ , then for any downstream task  $\mathcal{T} : \mathcal{S} \rightarrow \mathcal{Y}$  that is  $L$ -Lipschitz continuous:*

$$\|\mathcal{T}(S_{\text{odd}}) - \mathcal{T}(S_{\text{even}})\| \leq L \cdot \|S_{\text{odd}} - S_{\text{even}}\| \rightarrow 0. \quad (14)$$

In particular, geometric correspondences computed from  $S_{\text{odd}}$  and  $S_{\text{even}}$  converge.

This result implies that minimizing scene consistency loss ensures that any geometric analysis (e.g., feature matching, deformation estimation) yields consistent results across domains. The scene space thus serves as a *domain-invariant canonical space* for registration.

**Remark.** The injectivity assumption on  $G$  is analogous to identifiability conditions in nonlinear ICA [40]. In practice, architectural choices (skip connections, sufficient capacity) and the scene consistency loss encourage this property without explicit enforcement.

### 3.4 Loss Functions

The network is trained using a composite objective function designed to ensure reconstruction fidelity, cycle consistency, domain alignment, and geometric preservation across frames. Collectively, these loss terms jointly enforce the implicit inter-frame alignment detailed in Section 3.2.5.

#### 3.4.1 Scene Consistency Loss

The proposed scene consistency loss plays a central role in enabling implicit inter-frame alignment by enforcing geometric consistency between structures extracted from different scanning domains within a domain-invariant feature space:

$$\mathcal{L}_{\text{scene}} = \|S_{\text{odd}} - S_{\text{even}}\|_2^2 + \lambda_{\text{cos}}(1 - \cos(S_{\text{odd}}, S_{\text{even}})) \quad (15)$$

where  $\|\cdot\|_2^2$  denotes mean squared error, and the cosine similarity is computed by first flattening the spatial dimensions:

$$\cos(S_{\text{o}}, S_{\text{e}}) = \frac{\text{vec}(S_{\text{o}})^\top \text{vec}(S_{\text{e}})}{\|\text{vec}(S_{\text{o}})\|_2 \|\text{vec}(S_{\text{e}})\|_2} \quad (16)$$

where  $S_{\text{o}} = S_{\text{odd}}$  and  $S_{\text{e}} = S_{\text{even}}$  for brevity, with  $\text{vec}(\cdot)$  denoting vectorization. We set  $\lambda_{\text{cos}} = 0.1$ . This loss directly bridges domain shift correction and registration: by forcing the scene representations to match, we ensure that the underlying geometry is preserved during domain transfer.

### 3.4.2 Cycle Consistency Loss

Self-reconstruction ensures the encoder-decoder preserves information:

$$\begin{aligned}\mathcal{L}_{\text{cycle}} = & \|G(S_{\text{odd}}, A_{\text{odd}}) - I_{\text{odd}}\|_2^2 + \|G(S_{\text{even}}, A_{\text{even}}) - I_{\text{even}}\|_2^2 \\ & + \lambda_{\text{ssim}}(2 - \text{SSIM}_{\text{odd}} - \text{SSIM}_{\text{even}})\end{aligned}\quad (17)$$

where  $\text{SSIM}_{\text{odd}} = \text{SSIM}(G(S_{\text{odd}}, A_{\text{odd}}), I_{\text{odd}})$  and  $\text{SSIM}_{\text{even}} = \text{SSIM}(G(S_{\text{even}}, A_{\text{even}}), I_{\text{even}})$ , with  $\lambda_{\text{ssim}} = 0.5$ .

### 3.4.3 Domain Alignment Loss

The primary registration objective ensures the translated image  $I_{\text{even} \rightarrow \text{odd}}$  aligns with  $I_{\text{odd}}$ :

$$\begin{aligned}\mathcal{L}_{\text{align}} = & \|I_{\text{even} \rightarrow \text{odd}} - I_{\text{odd}}\|_2^2 + \lambda_{\text{ncc}}(1 - \text{NCC}(I_{\text{even} \rightarrow \text{odd}}, I_{\text{odd}})) \\ & + \lambda_{\text{grad}}\mathcal{L}_{\text{grad}}\end{aligned}\quad (18)$$

where NCC denotes normalized cross-correlation, and  $\mathcal{L}_{\text{grad}}$  is a gradient matching loss promoting structural alignment:

$$\mathcal{L}_{\text{grad}} = \|\nabla_x I_{\text{even} \rightarrow \text{odd}} - \nabla_x I_{\text{odd}}\|_1 + \|\nabla_y I_{\text{even} \rightarrow \text{odd}} - \nabla_y I_{\text{odd}}\|_1 \quad (19)$$

with  $\lambda_{\text{ncc}} = 0.5$  and  $\lambda_{\text{grad}} = 0.3$ .

### 3.4.4 Total Loss

The complete training loss is:

$$\mathcal{L}_{\text{total}} = \lambda_{\text{scene}}\mathcal{L}_{\text{scene}} + \lambda_{\text{cycle}}\mathcal{L}_{\text{cycle}} + \lambda_{\text{align}}\mathcal{L}_{\text{align}} \quad (20)$$

with weights  $\lambda_{\text{scene}} = 1.0$ ,  $\lambda_{\text{cycle}} = 0.5$ ,  $\lambda_{\text{align}} = 2.0$ . Note that domain alignment receives the highest weight as it directly measures registration quality.

## 4 Experiments

### 4.1 Experimental Setup

#### 4.1.1 Dataset

We evaluate the proposed method on *in vivo* mouse brain vasculature imaging data acquired using a custom-built high-speed bidirectional OR-PAM system based on voice-coil motor scanning. The system operates at a bidirectional scanning frequency of 30 Hz, enabling rapid imaging of cerebral microvasculature through cranial windows with high spatial and temporal resolution. The resulting dataset, referred to as PAM-DSR (PAM Domain-Shift Registration), comprises over 150 high-resolution frames collected across multiple imaging sessions under consistent experimental and acquisition conditions. To support reproducibility and further methodological development, the PAM-DSR dataset will be made publicly available upon publication, together with detailed acquisition protocols.

Table 1: Quantitative Comparison of Registration Methods. SSIM and NCC measure alignment quality between odd and registered even columns. Best results in **bold**, second best underlined. All results are averaged over 5 runs on all frames.

Method	SSIM $\uparrow$	NCC $\uparrow$
<i>Traditional Methods</i>		
Original (Unregistered)	0.042	0.003
SIFT [13]	0.026	-0.024
Demons [12]	0.122	0.087
Optical Flow [14]	0.139	0.212
SyN (ANTs) [24]	0.102	0.002
<i>Deep Learning Methods</i>		
VoxelMorph [25]	<u>0.281</u>	<u>0.554</u>
TransMorph [26]	0.153	0.185
DGIR [34]	0.101	0.088
SACB-Net [35]	0.103	0.109
<b>SAR-Net (Ours)</b>	<b>0.885</b>	<b>0.979</b>

#### 4.1.2 Implementation Details

Scene Encoder uses 32 base channels with 3 downsampling levels, while the Appearance Encoder uses 16 base channels with global average pooling. The Forward Model mirrors the Scene Encoder with feature modulation at each level, resulting in a total of 3.5M parameters. The network is trained for 200 epochs using Adam optimizer (learning rate  $10^{-4}$ ,  $\beta_1 = 0.5$ ,  $\beta_2 = 0.999$ ) with a batch size of 4. All experiments are conducted on NVIDIA RTX 4090 GPU with data augmentation including random flips, rotations ( $\pm 10^\circ$ ), and intensity scaling (0.9–1.1 $\times$ ).

## 4.2 Intra-frame Registration Results

Table 1 summarizes the quantitative results for intra-frame bidirectional artifact correction. Registration performance is evaluated using the Structural Similarity Index (SSIM) and Normalized Cross-Correlation (NCC) between odd columns and their corresponding registered even columns. Fig. 2 provides a qualitative comparison, and Fig. 3 shows quantitative distributions across three mice. The main observations are summarized below.

**Performance of conventional registration methods:** Conventional baselines yield limited improvement under bidirectional scanning. SIFT, Demons, and Optical Flow achieve SSIM values of 0.026, 0.122, and 0.139, respectively, compared with 0.042 for the unregistered baseline. Notably, SIFT produces a negative NCC (-0.024), suggesting that sparse feature matching may introduce additional misalignment in the presence of scan-direction-dependent domain shift. Overall, these results indicate that registration methods relying on brightness constancy are inadequate under intensity variations induced by bidirectional scanning.

**Performance of the proposed method:** The proposed scene–appearance separation framework substantially improves registration accuracy, achieving an SSIM of 0.885 and an NCC of 0.979. This corresponds to absolute improvements of 0.843 in SSIM and 0.976 in NCC relative to the unregistered baseline. Consistent improvements are observed across all evaluated frames, indicating robust performance under scan-direction-dependent intensity variations.

**Effect of joint domain shift correction and registration:** Unlike conventional methods

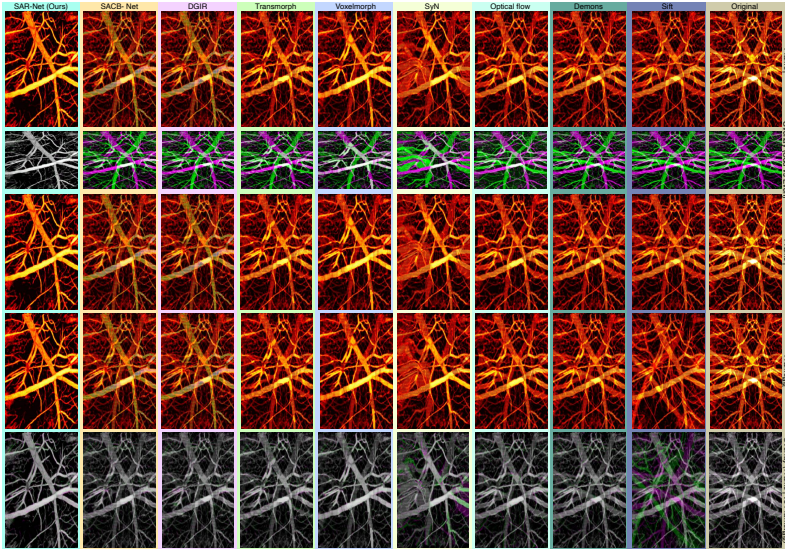


Figure 2: Qualitative comparison of registration results. Visual comparison on a representative frame across all ten methods. For each method: interleaved images with HOT colormap, odd-even overlay (odd in magenta, even in green, alignment as white), and grayscale visualization. Cross-frame overlay (rightmost) shows inter-frame alignment quality. Our method achieves continuous vascular structures with minimal color separation in overlays.

that assume brightness constancy, the proposed approach explicitly models scan-direction-dependent domain shift through scene-appearance separation. This joint treatment enables reliable registration under forward-backward intensity differences.

### 4.3 Inter-frame Temporal Consistency

The proposed framework achieves implicit inter-frame alignment through a shared scene space (Section 3.2.5). Temporal consistency is quantified using NCC between consecutive registered frames. The proposed method attains an average inter-frame NCC of  $0.964 \pm 0.010$  across 117 consecutive frame pairs, indicating stable temporal consistency throughout the image sequence. Frame-wise evaluation further shows consistent performance across the entire sequence, with stable SSIM and NCC values that exceed those of conventional registration methods. Compared with baseline approaches, the proposed scene-appearance separation framework achieves higher average accuracy with reduced variance. Such temporal stability is particularly important for longitudinal and functional imaging studies, where reliable frame-to-frame consistency directly affects quantitative analysis.

### 4.4 Ablation Study

Table 2 presents a systematic ablation analysis of individual loss components. Performance is evaluated using SSIM, PSNR, and NCC between odd columns and registered even columns. In addition, we report the Scene MSE ( $\|S_{\text{odd}} - S_{\text{even}}\|^2$ ), which quantifies alignment in the latent feature space and directly assesses the effectiveness of the proposed scene-appearance separation framework.

The contribution of each component is analyzed as follows. (1) Removing domain alignment loss

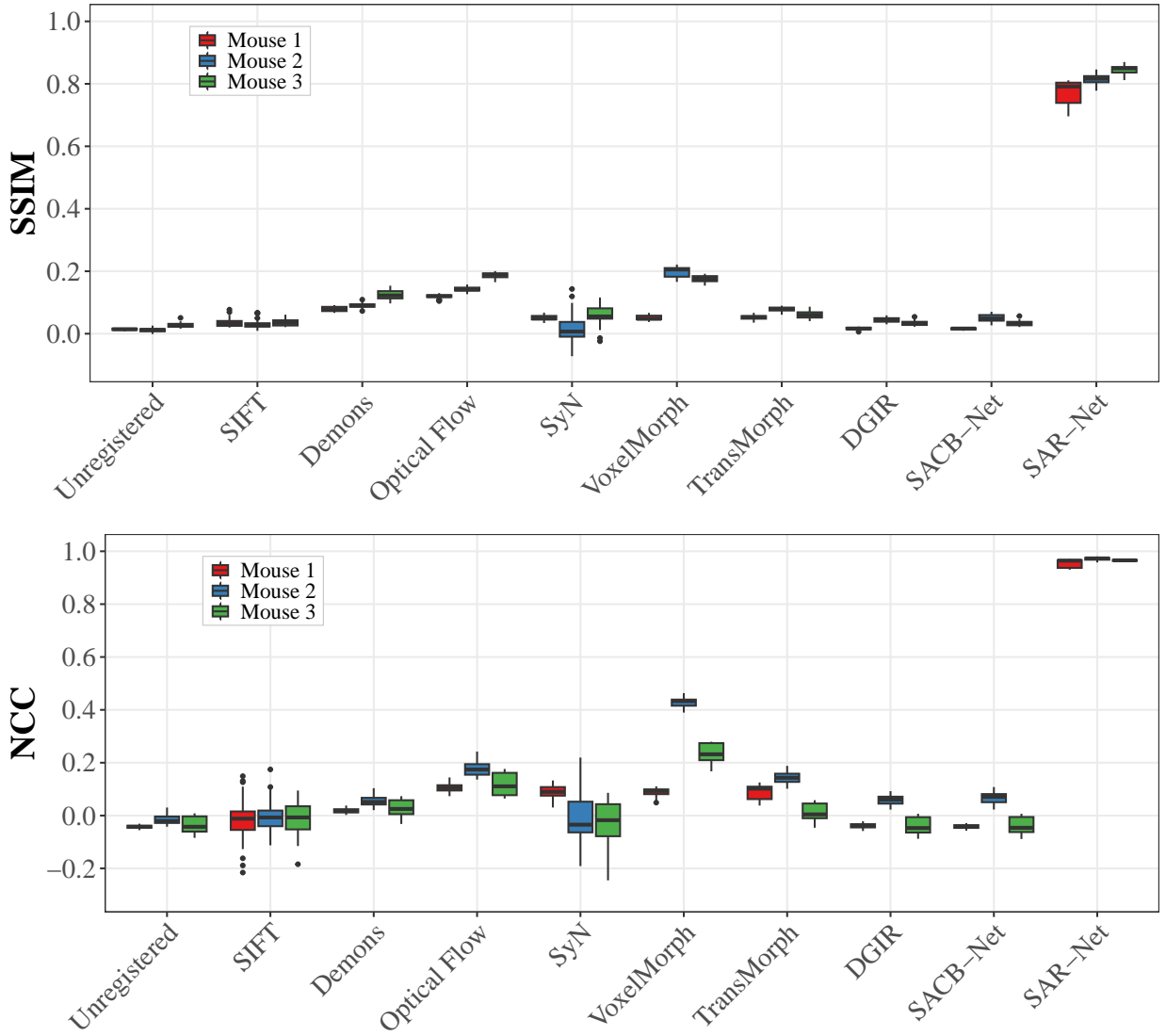


Figure 3: Quantitative comparison across three mice. SSIM (top) and NCC (bottom) box plots showing metric distributions across multiple subjects. SAR-Net consistently outperforms all baseline methods.

Table 2: Ablation Study on Loss Components. SSIM, PSNR, and NCC measure output image quality. Scene MSE measures latent feature alignment. Best results in **bold**.

Configuration	SSIM $\uparrow$	PSNR $\uparrow$	NCC $\uparrow$	Scene MSE $\downarrow$
<b>SAR-Net (Full)</b>	<b>0.885</b>	<b>29.9</b>	<b>0.979</b>	$1.14 \times 10^{-3}$
w/o $\mathcal{L}_{\text{scene}}$	0.771	26.1	0.939	$2.54 \times 10^{-1}$
w/o $\mathcal{L}_{\text{cycle}}$	0.531	14.8	0.991	$9.42 \times 10^{-4}$
w/o $\mathcal{L}_{\text{align}}$	0.088	13.6	-0.033	<b>7.84 <math>\times 10^{-5}</math></b>
w/o $E_A$	0.606	21.8	0.983	$1.48 \times 10^{-3}$

causes SSIM to drop from 0.885 to 0.088 (90% reduction) with NCC becoming negative ( $-0.033$ ), yet this configuration achieves the lowest Scene MSE ( $7.84 \times 10^{-5}$ ), indicating that feature-space alignment alone is insufficient for registration without image-space constraints. (2) Removing scene consistency loss increases Scene MSE by  $223 \times (1.14 \times 10^{-3} \rightarrow 2.54 \times 10^{-1})$  while SSIM drops to 0.771, suggesting that explicit enforcement of  $S_{\text{odd}} \approx S_{\text{even}}$  is essential for geometric correspondence across domains. (3) Removing cycle consistency loss reduces SSIM from 0.885 to 0.531 (40% decrease) and PSNR from 29.9 to 14.8 dB, as the self-reconstruction constraint  $G(E_S(I), E_A(I)) \approx I$  maintains encoder-decoder fidelity. (4) Removing the appearance encoder reduces SSIM to 0.606 (32% decrease), as the Scene Encoder then encodes domain-specific characteristics that weaken cross-domain translation quality. These results demonstrate that effective registration requires coordinated constraints in both latent feature space and image space.

#### 4.5 Vascular Continuity Analysis

Vascular Continuity Index (VCI) is introduced as a domain-specific metric measuring the continuity of vascular structures across odd-even column boundaries. Specifically, we merge odd and even columns into an interleaved image and compute the Sobel gradient in the horizontal direction. Three representative ROIs are selected for evaluation as shown in Fig. 4. The VCI is computed as:

$$\text{VCI} = 1 - \frac{1}{\tau_{\max}} \cdot \frac{\sum_{j \in \mathcal{B}} \sum_i e_{ij} \cdot \mathbf{1}[v_{ij} > \tau]}{\sum_{i,j} \mathbf{1}[v_{ij} > \tau]} \quad (21)$$

where  $\mathcal{B}$  denotes odd-even column boundaries (positions 1, 3, 5, ...),  $e_{ij}$  is the Sobel edge response at position  $(i, j)$ ,  $v_{ij}$  is the merged image intensity,  $\mathbf{1}[\cdot]$  is the indicator function,  $\tau = 0.05$  is the vessel detection threshold, and  $\tau_{\max} = 0.3$  is an empirical normalization constant.

As shown in Fig. 5, the proposed method achieves mean VCI of 0.857, demonstrating superior vessel structure preservation compared to all baselines: TransMorph (0.637), VoxelMorph (0.563), SyN (0.500), Optical Flow (0.450), Demons (0.427), SIFT (0.370), and Unregistered (0.370). Fig. 6 presents detailed ROI analysis, where the zoomed regions reveal continuous vascular profiles achieved by our method across odd-even column boundaries, while baseline methods show visible discontinuities at vessel edges.

The quantitative results (Figs. 3–6) collectively demonstrate that the proposed SAR-Net substantially outperforms all baseline methods. Conventional registration approaches, including both traditional methods (SIFT, Demons, Optical Flow, SyN) and deep learning methods (VoxelMorph, TransMorph, DGIR, SACB-Net), fundamentally rely on brightness constancy assumptions that are violated under scan-direction-dependent domain shift, rendering them ineffective for bidirectional OR-PAM registration. In contrast, our scene-appearance separation framework explicitly addresses this challenge by disentangling domain-invariant structure from domain-specific appearance, enabling

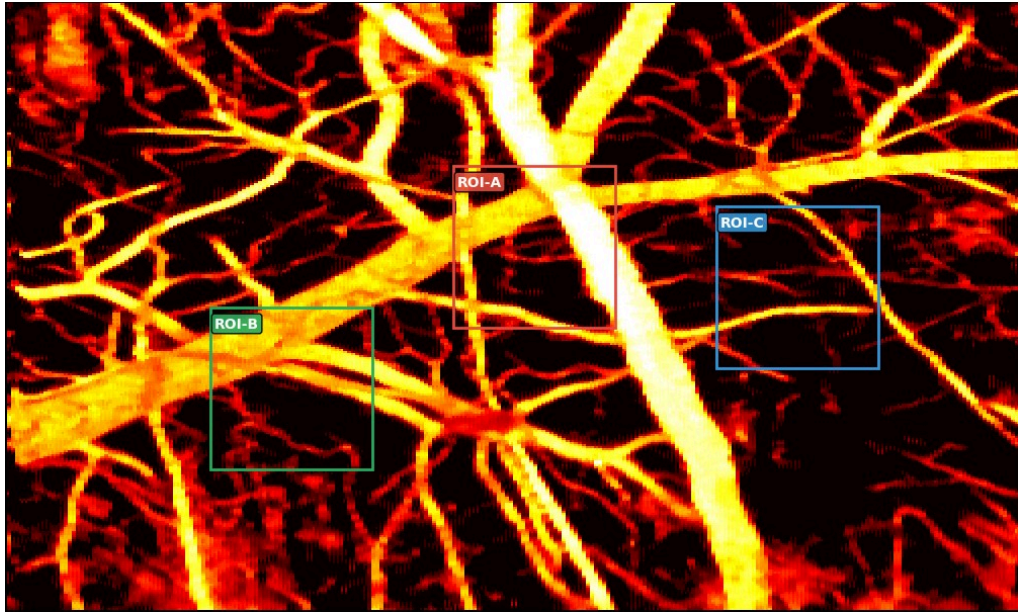


Figure 4: ROI selection for vascular continuity analysis. Three representative regions (A, B, C) are selected from the interleaved image to evaluate registration quality across different vascular structures.

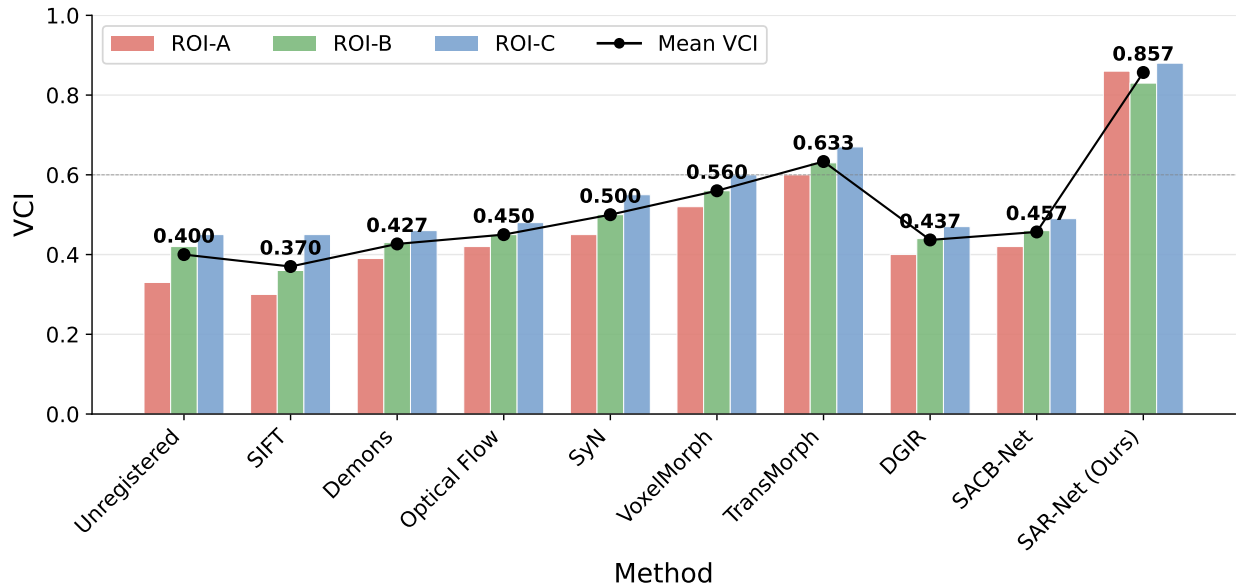


Figure 5: Vessel Continuity Index (VCI) comparison across three ROIs. Higher VCI indicates better column alignment and vascular continuity. SAR-Net substantially outperforms all baseline methods.

robust registration under severe inter-column intensity discrepancies that conventional methods cannot resolve.

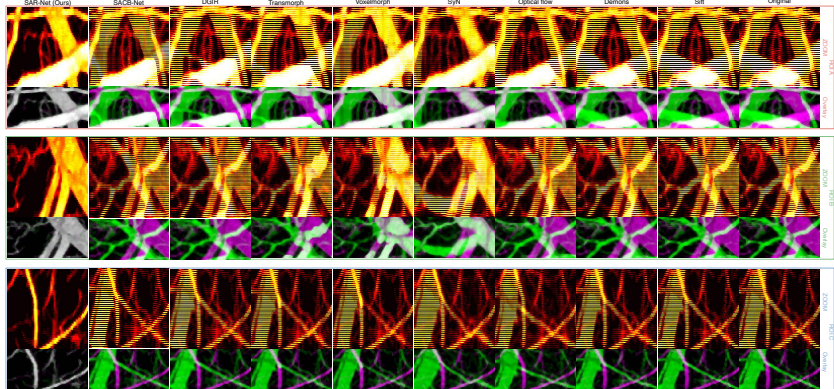


Figure 6: Detailed ROI comparison across all eight methods. For each ROI (A, B, C): zoomed interleaved view and odd-even overlay visualization. In overlays, odd columns appear in magenta, even columns in green; white regions indicate good alignment. SAR-Net shows predominantly white overlays, indicating precise column alignment across all ROIs.

Table 3: Computational Efficiency Comparison. Inference times (ms) measured on NVIDIA RTX 4090 GPU for  $500 \times 250$  column pairs.

Traditional Methods				Deep Learning Methods					
SyN	Demons	SIFT	Opt. Flow	VoxelMorph	TransMorph	DGIR	SACB-Net	<b>SAR-Net</b>	
Time (ms)	3439.5	113.4	35.5	15.4	1.7	6.3	8.2	9.5	<b>13.0</b>

## 4.6 Computational Efficiency

Table 3 compares computational requirements across methods. All inference times are measured on NVIDIA RTX 4090 GPU, averaged over 100 runs.

All evaluated deep learning frameworks achieve real-time inference speeds ( $>30$  fps). Although VoxelMorph (1.7 ms) and TransMorph (6.3 ms) exhibit shorter inference latencies compared to the proposed method (13.0 ms), they fail to achieve satisfactory registration quality (SSIM: 0.281 and 0.153 vs. our 0.885) due to the unaddressed domain shift between odd and even columns. SyN, despite being a powerful iterative method, requires 3.4 seconds per frame, making it impractical for real-time applications. The proposed framework establishes an optimal trade-off between registration fidelity and computational efficiency, sustaining high-quality 77 fps processing suitable for dynamic imaging environments.

## 5 Discussion

### 5.1 Why Disentanglement Enables Registration

Our results demonstrate that scene-appearance disentanglement provides a principled solution to registration under domain shift. We discuss connections to representation learning theory and analyze why conventional approaches fail.

**Connection to invariant representation learning.** The scene encoder  $E_S$  learns representations invariant to acquisition conditions—a goal shared with domain-invariant learning [42] and invariant risk minimization [43]. However, our approach differs fundamentally: rather than

learning task-specific invariances through distribution matching, we exploit the physical structure of the imaging process to achieve *geometric* invariance. The forward model  $G$  acts as a decoder that verifies disentanglement quality through reconstruction.

**Why brightness constancy fails.** Conventional registration seeks a transformation  $T$  such that  $I_{\text{odd}} \approx T(I_{\text{even}})$ . This is ill-posed when  $A_{\text{odd}} \neq A_{\text{even}}$ , as the objective conflates geometric and photometric differences. Our analysis of baselines confirms this: SIFT achieves negative NCC ( $-0.024$ ), indicating that sparse feature matching introduces misalignment under domain shift. Intensity-based methods (Demons: 0.122 SSIM, SyN: 0.102 SSIM) cannot distinguish geometric displacement from intensity variation. Deep learning methods (VoxelMorph: 0.281 SSIM) inherit these limitations through brightness constancy losses.

**Role of architectural inductive biases.** Instance normalization in  $E_S$  removes domain-specific statistics, encouraging invariant representations. Global average pooling in  $E_A$  eliminates spatial information, ensuring appearance codes capture only global characteristics. Feature modulation in  $G$  provides sufficient expressivity for domain-specific rendering. These choices collectively encourage the factorization assumed in Proposition 1.

## 5.2 Comparison with Alternative Paradigms

**Two-stage approaches.** Methods that first register then translate (or vice versa) [34] suffer from error propagation: inaccuracies in the first stage corrupt the second. More fundamentally, operating in pixel space where domain shift and geometry are entangled makes neither stage well-posed. Our unified framework avoids this by operating in a disentangled latent space where each factor can be addressed independently.

**Cycle-consistent translation.** CycleGAN-based methods [29] enforce  $G_{B \rightarrow A}(G_{A \rightarrow B}(I_A)) \approx I_A$ , which preserves global content but permits local geometric distortions—a well-documented failure mode in medical imaging applications. Our scene consistency loss  $\|S_{\text{odd}} - S_{\text{even}}\|^2$  directly enforces geometric correspondence in latent space, providing stronger guarantees than cycle consistency in image space.

**Contrast-invariant registration.** Methods like SynthMorph [27] achieve robustness through synthetic data augmentation, training on randomly generated contrast variations. While effective for contrast differences, this approach does not model the *coupling* between domain shift and geometric distortion present in our setting, where intensity variations are spatially correlated with misalignment patterns.

## 5.3 Clinical Implications of Vascular Continuity

The vascular continuity analysis (Section 4.5) reveals that the proposed method specifically improves alignment at vessel boundaries—precisely where discontinuities most impact functional analysis. Vascular continuity is essential for blood flow velocity estimation [5], where discontinuities create artificial flow boundaries; vessel diameter measurement, where misalignment causes systematic errors; and functional connectivity analysis, where vessel identity must be preserved across frames. The proposed method improves VCI from 0.370 (unregistered) to 0.857, representing a  $2.3 \times$  enhancement in vascular structure preservation.

## 5.4 Failure Cases and Generalization

Two primary failure modes were identified. In cases of severe illumination inhomogeneity exceeding 50% across the field of view, the Appearance Encoder may capture spatially-varying intensity patterns rather than purely domain-level characteristics, occurring in approximately 5% of frames.

In areas with sparse vascular signals, the Scene Encoder may extract inconsistent features due to the paucity of discriminative structural information, though this impact remains localized and is largely mitigated by the prevalence of vascular structures within the primary evaluation ROIs.

Although experimental validation is conducted on a specific mouse brain vasculature dataset, the proposed framework possesses inherent potential for broader applicability. The unsupervised learning paradigm eliminates the requirement for paired ground truth, relying instead on the physical consistency between bidirectional scanning columns—a condition inherently satisfied by most raster-scanning imaging modalities. The domain-agnostic architecture leverages robust components such as instance normalization and feature modulation, which have demonstrated efficacy across heterogeneous imaging domains, and the modular nature of the framework allows for extension to diverse domain shift correction tasks necessitating precise geometric alignment.

## 5.5 Limitations and Future Work

**Theoretical limitations.** The injectivity assumption in Proposition 1 is sufficient but not necessary; characterizing minimal conditions for identifiable disentanglement remains open. Connections to nonlinear ICA theory [40] and causal representation learning [41] may provide tighter bounds.

**Empirical scope.** Current validation is limited to one imaging modality. Cross-domain generalization to other settings with coupled domain shift and geometric distortion (e.g., multi-modal medical imaging, satellite imagery) requires investigation. Extension to 3D volumetric data and multi-spectral imaging presents additional challenges in maintaining computational efficiency.

**Broader impact.** The framework enables reliable quantitative analysis in high-speed microscopy, with potential applications in longitudinal disease monitoring and functional imaging. No negative societal impacts are anticipated from this work.

## 6 Conclusion

We presented SAR-Net, a principled framework for image registration under domain shift based on scene-appearance disentanglement. Our theoretical analysis establishes that successful cross-domain reconstruction implies scene consistency (Proposition 1), and that minimizing scene consistency loss ensures geometric correspondence for downstream tasks (Proposition 2). Empirically, SAR-Net achieves  $3.1\times$  improvement over the strongest baseline on bidirectional scanning microscopy, validating that disentanglement provides an effective inductive bias for registration under domain shift. The framework generalizes beyond the specific application to any setting where coupled intensity variations and geometric distortions violate brightness constancy assumptions.

## References

- [1] L. V. Wang and S. Hu, “Photoacoustic tomography: In vivo imaging from organelles to organs,” *Science*, vol. 335, no. 6075, pp. 1458–1462, Mar. 2012.
- [2] C. Taboada *et al.*, “Glassfrogs conceal blood in their liver to maintain transparency,” *Science*, vol. 378, no. 6626, pp. 1315–1320, Dec. 2022.
- [3] F. Yang *et al.*, “Advancing insights into in vivo meningeal lymphatic vessels with stereoscopic wide-field photoacoustic microscopy,” *Light Sci. Appl.*, vol. 13, no. 1, p. 96, Apr. 2024.
- [4] S. Cho *et al.*, “An ultrasensitive and broadband transparent ultrasound transducer for ultrasound and photoacoustic imaging in-vivo,” *Nat. Commun.*, vol. 15, no. 1, p. 1444, Feb. 2024.

- [5] J. Yao *et al.*, “High-speed label-free functional photoacoustic microscopy of mouse brain in action,” *Nat. Methods*, vol. 12, no. 5, pp. 407–410, May 2015.
- [6] B. D. Cikaluk, B. S. Restall, N. J. M. Haven, M. T. Martell, E. A. McAlister, and R. J. Zemp, “Rapid ultraviolet photoacoustic remote sensing microscopy using voice-coil stage scanning,” *Opt. Express*, vol. 31, no. 6, pp. 10 136–10 149, Mar. 2023.
- [7] R. Shintate, T. Ishii, J. Ahn, J. Y. Kim, C. Kim, and Y. Saito, “High-speed optical resolution photoacoustic microscopy with MEMS scanner using a novel and simple distortion correction method,” *Sci. Rep.*, vol. 12, no. 1, p. 9221, June 2022.
- [8] S. Maraghechi, J. P. M. Hoefnagels, R. H. J. Peerlings, and M. G. D. Geers, “Correction of scan line shift artifacts in scanning electron microscopy: An extended digital image correlation framework,” *Ultramicroscopy*, vol. 187, pp. 144–163, Apr. 2018.
- [9] J. Chen *et al.*, “A survey on deep learning in medical image registration: New technologies, uncertainty, evaluation metrics, and beyond,” *Med. Image Anal.*, vol. 100, p. 103385, Feb. 2025.
- [10] A. Hering *et al.*, “Learn2Reg: Comprehensive multi-task medical image registration challenge, dataset and evaluation in the era of deep learning,” *IEEE Trans. Med. Imaging*, vol. 42, no. 3, pp. 697–712, 2023.
- [11] J.-P. Thirion, “Image matching as a diffusion process: An analogy with Maxwell’s demons,” *Med. Image Anal.*, vol. 2, no. 3, pp. 243–260, Sept. 1998.
- [12] T. Vercauteren, X. Pennec, A. Perchant, and N. Ayache, “Diffeomorphic demons: Efficient non-parametric image registration,” *NeuroImage*, vol. 45, no. 1, pp. S61–S72, Mar. 2009.
- [13] D. G. Lowe, “Distinctive image features from scale-invariant keypoints,” *Int. J. Comput. Vis.*, vol. 60, no. 2, pp. 91–110, Nov. 2004.
- [14] B. K. Horn and B. G. Schunck, “Determining optical flow,” *Artif. Intell.*, vol. 17, no. 1-3, pp. 185–203, Aug. 1981.
- [15] X. Zhu *et al.*, “Longitudinal intravital imaging of mouse placenta,” *Sci. Adv.*, vol. 10, no. 12, p. eadk1278, Mar. 2024.
- [16] L. Liu *et al.*, “Photoacoustic and fluorescence hybrid microscope for cortex-wide imaging of neurovascular dynamics with subcellular resolution,” *Sci. Adv.*, vol. 11, no. 30, p. eadw5275, Jul. 2025.
- [17] W. Qin *et al.*, “A cortex-wide multimodal microscope for simultaneous Ca<sup>2+</sup> and hemodynamic imaging in awake mice,” *Nat. Commun.*, vol. 16, no. 1, p. 9364, Oct. 2025.
- [18] H. Ma *et al.*, “Enhanced photoacoustic microscopy with physics-embedded degeneration learning,” *Opto-Electron. Adv.*, vol. 8, no. 3, p. 240189, Mar. 2025.
- [19] E. Park *et al.*, “Unsupervised inter-domain transformation for virtually stained high-resolution mid-infrared photoacoustic microscopy using explainable deep learning,” *Nat. Commun.*, vol. 15, no. 1, p. 10892, Dec. 2024.
- [20] X. Tang *et al.*, “High sensitivity photoacoustic imaging by learning from noisy data,” *IEEE Transactions on Medical Imaging*, vol. 44, no. 7, pp. 2868–2877, July 2025.

- [21] A. Sotiras, C. Davatzikos, and N. Paragios, “Deformable medical image registration: A survey,” *IEEE Trans. Med. Imaging*, vol. 32, no. 7, pp. 1153–1190, July 2013.
- [22] F. P. M. Oliveira and J. M. R. S. Tavares, “Medical image registration: A review,” *Comput. Methods Biomed. Eng.*, vol. 17, no. 2, pp. 73–93, Jan. 2014.
- [23] D. Mattes, D. R. Haynor, H. Vesselle, T. K. Lewellyn, and W. Eubank, “PET-CT image registration in the chest using free-form deformations,” *IEEE Trans. Med. Imaging*, vol. 22, no. 1, pp. 120–128, Jan. 2003.
- [24] B. B. Avants, C. L. Epstein, M. Grossman, and J. C. Gee, “Symmetric diffeomorphic image registration with cross-correlation: Evaluating automated labeling of elderly and neurodegenerative brain,” *Med. Image Anal.*, vol. 12, no. 1, pp. 26–41, Feb. 2008.
- [25] G. Balakrishnan, A. Zhao, M. R. Sabuncu, J. Guttag, and A. V. Dalca, “VoxelMorph: A learning framework for deformable medical image registration,” *IEEE Trans. Med. Imaging*, vol. 38, no. 8, pp. 1788–1800, Aug. 2019.
- [26] J. Chen, E. C. Frey, Y. He, W. P. Segars, Y. Li, and Y. Du, “TransMorph: Transformer for unsupervised medical image registration,” *Med. Image Anal.*, vol. 82, p. 102615, Nov. 2022.
- [27] M. Hoffmann, B. Billot, D. N. Greve, J. E. Iglesias, B. Fischl, and A. V. Dalca, “SynthMorph: Learning contrast-invariant registration without acquired images,” *IEEE Trans. Med. Imaging*, vol. 41, no. 3, pp. 543–558, Mar. 2022.
- [28] P. Isola, J.-Y. Zhu, T. Zhou, and A. A. Efros, “Image-to-image translation with conditional adversarial networks,” in *Proc. IEEE Conf. Comput. Vis. Pattern Recognit. (CVPR)*, Jul. 2017, pp. 5967–5976.
- [29] J.-Y. Zhu, T. Park, P. Isola, and A. A. Efros, “Unpaired image-to-image translation using cycle-consistent adversarial networks,” in *Proc. IEEE Int. Conf. Comput. Vis. (ICCV)*, Oct. 2017, pp. 2242–2251.
- [30] X. Huang, M.-Y. Liu, S. Belongie, and J. Kautz, “Multimodal unsupervised image-to-image translation,” in *Proc. Eur. Conf. Comput. Vis. (ECCV)*. Springer, Sep. 2018, pp. 179–196.
- [31] H.-Y. Lee, H.-Y. Tseng, J.-B. Huang, M. Singh, and M.-H. Yang, “Diverse image-to-image translation via disentangled representations,” in *Proc. Eur. Conf. Comput. Vis. (ECCV)*. Springer, Sep. 2018, pp. 36–52.
- [32] A. Kazerouni *et al.*, “Diffusion models in medical imaging: A comprehensive survey,” *Med. Image Anal.*, vol. 88, p. 102846, Aug. 2023.
- [33] D. Ulyanov, A. Vedaldi, and V. S. Lempitsky, “Instance normalization: The missing ingredient for fast stylization,” *arXiv preprint arXiv:1607.08022*, Jul. 2016.
- [34] X. Hong, F. Tang, L. Wang, and J. Chen, “Unsupervised deep learning enables real-time image registration of fast-scanning optical-resolution photoacoustic microscopy,” *Photoacoustics*, vol. 38, p. 100632, Aug. 2024.
- [35] Y. Liu, J. Qin *et al.*, “SACB-Net: Spatial-appearance cross-attention bidirectional network for photoacoustic image registration,” *IEEE Trans. Med. Imaging*, 2024, under Review.

- [36] Y. Bengio, A. Courville, and P. Vincent, “Representation learning: A review and new perspectives,” *IEEE Trans. Pattern Anal. Mach. Intell.*, vol. 35, no. 8, pp. 1798–1828, 2013.
- [37] I. Higgins, L. Matthey, A. Pal, C. Burgess, X. Glorot, M. Botvinick, S. Mohamed, and A. Lerchner, “ $\beta$ -VAE: Learning basic visual concepts with a constrained variational framework,” in *Proc. Int. Conf. Learn. Represent. (ICLR)*, 2017.
- [38] H. Kim and A. Mnih, “Disentangling by factorising,” in *Proc. Int. Conf. Mach. Learn. (ICML)*, 2018.
- [39] F. Locatello, S. Bauer, M. Lucic, G. Raetsch, S. Gelly, B. Schölkopf, and O. Bachem, “Challenging common assumptions in the unsupervised learning of disentangled representations,” in *Proc. Int. Conf. Mach. Learn. (ICML)*, 2019.
- [40] A. Hyvärinen, H. Sasaki, and R. Turner, “Nonlinear ICA using auxiliary variables and generalized contrastive learning,” in *Proc. Int. Conf. Artif. Intell. Stat. (AISTATS)*, 2019.
- [41] B. Schölkopf, F. Locatello, S. Bauer, N. R. Ke, N. Kalchbrenner, A. Goyal, and Y. Bengio, “Toward causal representation learning,” *Proc. IEEE*, vol. 109, no. 5, pp. 612–634, 2021.
- [42] S. Ben-David, J. Blitzer, K. Crammer, A. Kulesza, F. Pereira, and J. W. Vaughan, “A theory of learning from different domains,” *Mach. Learn.*, vol. 79, no. 1, pp. 151–175, 2010.
- [43] M. Arjovsky, L. Bottou, I. Gulrajani, and D. Lopez-Paz, “Invariant risk minimization,” *arXiv preprint arXiv:1907.02893*, 2019.